Real-Time Temperature Control and Performance Optimization of an Induction Heating System for In-Situ Neutron Experiments*

Yaojun Guan,[1,2,†] Bin Li,[2,3,4,†] Haoran Chen,[5,2,4,†] Linjin Deng,[2,6,4] Wenbin Zhong,[2,4,3] Fan Ye,[2,4,3] Mengjia Dou,[2,4,3] Bo Bai,[2,4,3] Xiaohu Li,[2,4,3] Yi Zhang,[1] Xiaoyue Zhang,[1] Xinzhi Liu,[1] Mengyu He,[7,2] Hui Cheng,[2,4,3,‡] Haitao Hu,[2,4,3,§] and Xin Tong[2,4,3,¶]

[1]*Guangdong Provincial Key Laboratory of Magnetoelectric Physics and Devices, School of Physics, Sun Yat-sen University, Guangzhou 510275, China*
[2]*Spallation Neutron Source Science Center, Dongguan, 523803, China*
[3]*Institute of High Energy Physics, Chinese Academy of Sciences (CAS), Beijing, 100049, China*
[4]*Guangdong Provincial Key Laboratory of Extreme Conditions, Dongguan, 523803, China*
[5]*Northeastern University, No3-11 Wenhua Road, Heping District, Shenyang, Liaoning, 110819, China*
[6]*Dongguan University of Technology, Dongguan, 523808, China*
[7] *University of California, Merced 5200 North Lake Rd, Merced, CA 95343, United States*

Induction heating is an non-contact heat source widely used in advanced thermal manufacturing and in-situ high-temperature characterization, yet conventional low-/mid-frequency systems suffer from large skin depth and diffuse energy deposition,which limits heating rate and spatial localization. To overcome this limitation, we developed a high-frequency, high-current synergistic intensification strategy. The inverter frequency is elevated to the hundred-kilohertz range and paired with a large-current zero-current-switching (ZCS) IGBT series-resonant converter. This configuration compresses electromagnetic energy into a sub-millimetre surface layer, yielding a marked increase in both heat-flux density and heating rate. A full-digital phase-locked loop together with dual-redundant protection guarantees stable high-current output at elevated frequencies. Theoretical analysis, multi-physics simulations, and comparative experiments consistently demonstrate that the system can rapidly and uniformly heat the work-piece surface to the target temperature, offering an efficient, controllable and mobile heat source for low-carbon and precision thermal treatments.

Keywords: High frequency induction heating; Rapid heating; Precision temperature control; Force thermal in-situ loading

I. INTRODUCTION

Understanding the mechanical behavior and microstructural evolution of materials under extreme thermal conditions is a central challenge in aerospace, automotive manufacturing, and energy applications [1, 2]. Neutron scattering technology [3] not only plays an important role in fields such as physics [4, 5], biology [6], archaeology [7], and chemistry [8], but also serves as a crucial detection and analysis tool in the field of materials science research [9, 10].Neutron diffractometers are especially valuable for probing microstructure and mechanical behavior under both ambient and high-temperature conditions [11–13]. With the growing focus on transient non-equilibrium processes, rapid heating has become a widely adopted method in high-temperature material research for simulating extreme thermal loads.To achieve real-time dynamic monitoring of materials under extreme high-temperature conditions, especially to precisely capture of mechanical responses and microstructure evolution during the rapid heating process [14], the coupling of neutron instruments with thermomechanical loading systems—particularly heating devices with rapid temperature rise capabilities—has become increasingly crucial [15, 16].

Traditional heating devices mainly include infrared heating and resistance heating [17, 18]. Among these, resistance heating primarily raises the sample temperature by leveraging the inherent electrical resistance of the material [19, 20], while infrared heating mainly relies on the principle of thermal radiation to indirectly heat materials [21, 22].Resistance heating typically exhibits low heating and cooling rates, which leads to prolonged experimental cycles [23, 24]. Moreover, different types of resistance wires have distinct operating temperature ranges, and they are prone to oxidation at high temperatures, which results in short service lives of heating elements and restricts the temperature range for high-temperature experiments [25, 26].Infrared heating, however, suffers from nonuniform temperature field and limited temperature-control accuracy. Additionally, due to the diversity of test materials, it shows poor heating efficiency when dealing with materials that have low infrared absorption rates [27, 28].

As a non-contact, efficient, and controllable heating technology, induction heating has gradually replaced traditional heating methods in recent years and become one of the primary heating means in high-temperature material research [29, 30]. A key advantage of induction heating is that the energy is delivered directly on the target, which significantly reduces heat loss, improves heating efficiency and shortens the

* This work was supported by the National Key R&D Program of China (No. 2022YFA1604104), the Youth Innovation Promotion Association of the Chinese Academy of Sciences, the National Natural Science Foundation of China (12427803, 12425512, and 12575323), the Guangdong Provincial Key Laboratory of Magnetoelectric Physics and Devices (No. 2022B1212010008), the Research Center for Magnetoelectric Physics of Guangdong Province (2024B0303390001), and the Guangdong Provincial Key Laboratory of Extreme Conditions (2023B1212010002).
† The authors contribute equally.
‡ Corresponding author,chenghui@ihep.ac.cn
§ Corresponding author,huht@ihep.ac.cn
¶ Corresponding author,tongxin@ihep.ac.cn

heating duration [31, 32].Furthermore, by adjusting the coil geometry and control systems parameter, induction heating can precisely regulate the heating area and the temperature gradient to meet specific experimental requirements. This enables it to meet the stringent requirements for heating precision and dynamic response in high-temperature material research [33, 34].

Recently, a variety of high-temperature heating technologies have been applied into neutron diffractometer experiments to support precise material testing in elevated temperature. The ENGIN-X instrument at the ISIS Laboratory employs an infrared-heated high-temperature furnace, equipped with four 2 kW infrared heaters, and its maximum heating temperature can reach up to 1373 K [35, 36].By contrast, the VULCAN instrument at the SNS Laboratory in the United States integrates three heating devices, including a standalone high-temperature furnace, a resistance-heated gas-tight load frame furnace, and an auxiliary induction heating coil. These devices can reach temperature up to 1600 °C; among them, the resistance-heated gas-tight load frame furnace features a relatively high heating rate, capable of achieving a temperature rise of up to 600 °C/s [37].At the J-PARC Laboratory in Japan, the PLANET instrument employs a heater powered by embedded high-voltage batteries, with a maximum achievable temperature of 2000 K. In contrast, the TAKUMI instrument uses an infrared heating device, which is limited to a maximum heating temperature of 1273 K [38].

At the China Spallation Neutron Source (CSNS) ,the current high-temperature sample environment systems include a pulsed laser heating furnace and an ultra-high-temperature induction heating device . The pulsed laser heating furnace has a rated output power range of 100 - 2000 W, a maximum controllable heating temperature of 1800 °C, and a heating rate ranging from 80 °C/s - 150 °C/s [39].The induction heating device, by contrast, can reach 2700 K with a heating power of 60 kW, placing it among the highest-temperatures induction furnaces currently reported in this field [40].However, this induction heating device is primarily used for research on high-temperature microstructures and macroscopic properties, and it cannot meet the requirements of experiments such as strain measurement [41] and residual stress distribution measurement [42].These experiments require rapid heating to minimize stress relaxation and microstructural changes during temperature ramping, as well as precise temperature control to avoid thermal gradients that introduce artifacts in strain measurements.

Addressing the insufficiency of existing heating devices in rapid temperature rise capability, this study focuses on key technical issues such as the optimization of high-frequency induction technology, enhancement of thermal field uniformity, and intelligentization of temperature control systems, and proposes an innovative rapid temperature rise induction heating scheme. This scheme aims to significantly improve heating rate, temperature control accuracy, and thermal field stability, thereby meeting the requirements of diffractometer experiments—including those for material dynamic response, strain measurement, and residual stress analysis—under high-temperature conditions. To verify the feasibility and performance advantages of this scheme, this paper combines theoretical modeling and experimental testing to conduct a systematic evaluation of the system from multiple dimensions, including electromagnetic coupling, heat transfer behavior, and temperature control feedback response.

The implementation of this research not only helps to improve the overall experimental efficiency and testing accuracy of neutron diffractometers, but also provides strong technical support for the accurate investigation of the service behavior of materials in complex thermo-mechanical environments, thus carrying important theoretical and engineering application value.

II. INTRODUCTION TO THE OVERALL DESIGN AND MECHANISM OF THE INSTRUMENT

Fig. 1 illustrates an innovative coupling design that integrates an advanced engineering large-sample loading device with induction heating equipment, providing a versatile experimental platform for materials science research. This platform is capable of simultaneously applying stress and induction heating to materials, effectively simulating the complex environmental conditions encountered in practical applications. To address the limitations of existing heating devices in terms of rapid temperature increase capabilities, we will delve into the principles of induction heating technology, focusing on the optimization of high-frequency induction techniques, enhancement of thermal field uniformity, and the intelligent control of temperature systems, with the aim of significantly improving heating efficiency and precision, thereby better serving research and development in the field of materials science.

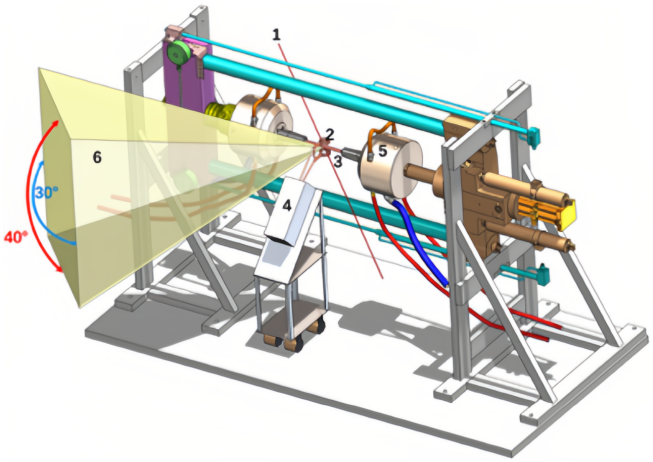

Fig. 1. Engineering Material Diffractometer coupled with induction heating equipment design diagram: 1) neutron beam, 2) induction heating coil, 3) test workpiece, 4) induction heating water-cooled module, 5) stress loader clamping head, 6) neutron scattering space angle.

Induction heating technology is based on the principle of electromagnetic induction. When an alternating current i

flows through the induction coil, it generates an alternating magnetic field within the coil. A workpiece placed within this alternating magnetic field experiences an induced electromotive force e, which in turn gives rise to eddy currents within the workpiece. Due to the eddy current effect and the inherent equivalent resistance R of the metal material, thermal energy is generated internally, thereby achieving the goal of heating the workpiece.

During the heating process, induction heating transfers electrical energy from the induction coil to the metallic workpiece, which is then converted into thermal energy within the workpiece itself. This energy transfer is accomplished via electromagnetic induction, without direct physical contact between the coil and the workpiece. As such, induction heating is classified as a non-contact heating method. The working process diagram of induction heating is shown in Fig. 2 .

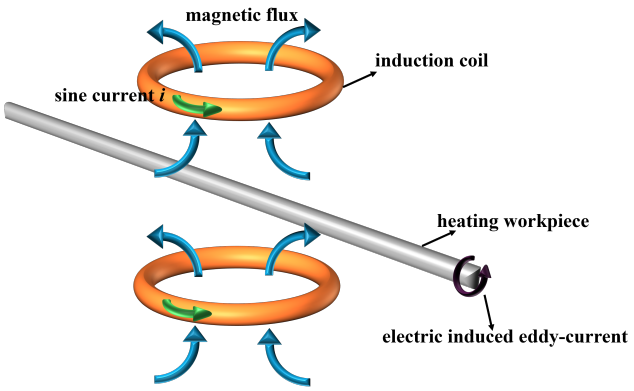

Fig. 2. Induction heating operation diagram.

When the sinusoidal current i in the induction coil varies at a specific frequency, the resulting alternating magnetic field generated within the coil will exhibit the same frequency as the input current. This time-varying magnetic field induces a magnetic flux Φ through the workpiece, which can be expressed by the following formula [43],

$$\Phi = \Phi_m \sin(\omega t) \tag{1}$$

Where Φ is the magnetic flux in the induction coil; Φ_m is the amplitude of the alternating flux; and ω is the current angular frequency. The alternating magnetic flux generated by the induction coil induces an electromotive force (EMF) e in the workpiece via the principle of electromagnetic induction. This induced EMF can be described by Faraday's law as follows,

$$e = -N\frac{d\Phi}{dt} \tag{2}$$

Where e is the induced electromotive force,and N is the equivalent number of turns of the workpiece. Substituting Eq. (1) into Eq. (2) gives the induced electromotive force as follows,

$$e = -N\Phi_m\omega\cos(\omega t) \tag{3}$$

The Root Mean Square value of the induced electromotive force is then given by:

$$E = \frac{N\Phi_m\omega}{\sqrt{2}} = \frac{2\pi f N\Phi_m}{\sqrt{2}} = 4.44Nf\Phi_m \tag{4}$$

Where E is the effective value of the induced electromotive force,and f is the frequency of the energizing current of the induction coil. The induction electromotive force drives current within the metal workpiece and thereby generates the Joule heat during heating. The generated heat can be expressed as:

$$\begin{aligned} Q &= 0.24Pt = 0.24I^2Rt \\ &= \frac{0.24E^2}{Z^2}Rt \\ &= \frac{4.73f^2N^2\Phi_m^2Rt}{Z^2} \end{aligned} \tag{5}$$

Where Q is the generated Joule heat in calories (cal), P is the output power of the induction heating device, t is the energization time of the induction coil when the metal workpiece is heated, I is the rms value of the induction current, R is the equivalent resistance of the metal workpiece, and Z is the equivalent impedance modulus of the metal workpiece.

According to the equations above, when the properties and geometry of the metal workpiece remain unchanged, the amount of heat generated within the workpiece depends primarily on the frequency f of the current supplied to the induction coil, as well as the magnetic flux. The magnetic flux itself is determined by multiple factors, including the magnitude of the current flowing through the coil, the number of turns in the heating coil, and its spatial orientation relative to the workpiece.

Therefore, for a given metal workpiece, the heating power delivered by the induction heating system can be effectively adjusted by altering the excitation frequency, the coil current, the number of coil turns, or the position of the coil with respect to the workpiece. These parameters collectively govern the efficiency and intensity of electromagnetic induction and thus play a crucial role in controlling the thermal behavior of the system.

Based on this analysis, the paper proposes and verifies an "HF-Large Current"(High-Frequency Large Current) collaborative enhancement instrument design scheme: The inverter switching frequency is extended from the commonly used 10-30 kHz to 110 kHz. The system uses a 110 kHz large current ZCS-IGBT (Zero-Current Switching Insulated Gate Bipolar Transistor) series resonance with 33 ns DSP(Digital Signal Processor) all-digital phase-locking, achieving an efficiency of $\geq 95\%$ and a power factor of ≥ 0.87. The dual-channel redundancy and 5 μs hardware protection ensure a 99.9% availability. It also includes a built-in 4–20 mA temperature closed-loop and segmented programming, with a temperature control accuracy of 1%FS(Full Scale), providing a high-efficiency and highly reliable integrated heat source for high-power mobile output scenarios.

The prototype induction heating device designed using the "high-frequency - large current" collaborative enhancement

concept is shown in Fig. 3 . The system is built with a PID(Proportional-Integral-Derivative) closed-loop control for accurate temperature management. The temperature reading is done using a K-type thermocouple fixed to the test workpiece, with the option of replacing it with an infrared thermometer if needed. This design ensures precision and flexibility, adapting to various heating processes with reliable, real-time feedback and control.

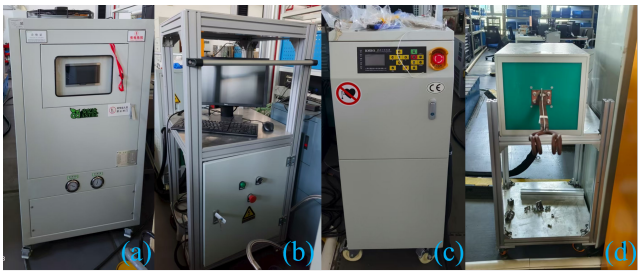

Fig. 3. Induction heating systems: (a) water-cooled chassis; (b) host computer; (c) power control; (d) induction heating coils and transformer.

By significantly increasing the frequency from 30 kHz to 110 kHz, the system achieves a heating rate of up to 200°C/s, reducing the high-temperature dwell time from several tens of seconds to just a few seconds. This rapid thermal response provides reproducible and instantaneous temperature profiles for in-situ loading experiments. The combination of fast heating and precise temperature control enables material behavior studies under dynamic thermo-mechanical coupling conditions, offering enhanced temporal resolution and data reliability. Additionally, the reduction in heating time and convection-radiation losses leads to a decrease in overall energy consumption. Significant synergistic optimization is achieved in process precision and characterization data quality, realizing the transition from traditional prolonged heating to an instantaneous, precise, and energy-efficient heating mode.

III. INDUCTION HEATING SIMULATION

To investigate the coupling mechanism between the electromagnetic field and the temperature field within a metal workpiece during the induction heating process, a three-dimensional model was established using the COMSOL Multiphysics simulation platform, as shown in Fig. 4. This model systematically simulates the electromagnetic-thermal interactions between the induction coil and the cylindrical metal workpiece. The geometry includes the induction coil, the workpiece, and the surrounding air domain. An insulation gap is defined between the coil and the workpiece to replicate the actual non-contact heating scenario. See Table 1 and Table 2 for model-related geometric parameters.

The simulation employs the “Magnetic Fields” and “Heat Transfer in Solids” physics interfaces, with a fully coupled solution approach to ensure real-time feedback between the electromagnetic excitation and thermal response. The induction coil is excited by a sinusoidal alternating current with a frequency of 110 kHz and a current amplitude of 700 A. The coil is made of a highly conductive metal. To prevent excessive temperature rise in the coil during continuous operation, an internal water-cooling channel is incorporated into the model. This is implemented by defining a fluid domain within the coil and applying either a constant temperature boundary condition or a forced convection condition to simulate the flow of cooling water. The cooling system ensures thermal stability of the coil during operation and enhances the overall heating efficiency and reliability of the simulation.

TABLE 1. Induction coil parameters

coil geometry	parameters
number of turns of coil (turns)	3
coil spacing (mm)	7
distance between two coils (mm)	20
large coil radius (mm)	25
radius of the metal tube of the induction coil (mm)	3

TABLE 2. Parameters of heated samples

heated bar geometry	parameters
radius (mm)	5
length (mm)	100
thermal conductivity W/(m·K)	57

The inlet temperature of the cooling water is set to $10°C$, with a mass flow rate of $0.01\,\mathrm{kg/s}$. This thermal management strategy plays a critical role in maintaining coil performance and ensuring accurate prediction of the thermal field distribution in the workpiece.

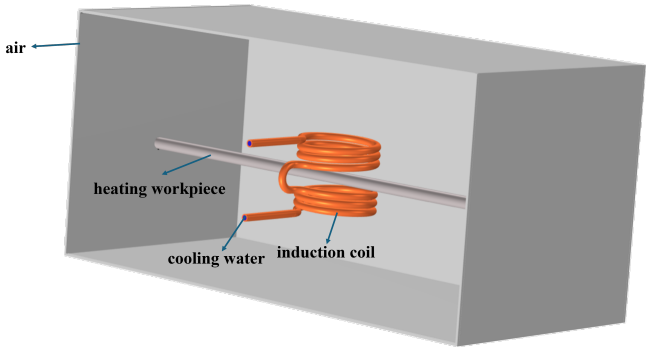

Fig. 4. Induction heating geometry model.

The simulated metal material is tantalum. In terms of material properties, the workpiece was assigned temperature-dependent parameters, including electrical conductivity, thermal conductivity, specific heat capacity, and density. These properties were implemented in COMSOL via interpolation functions to ensure accurate modeling of the material response under high-temperature conditions.

To better reflect realistic thermal boundary conditions, natural convection was applied to the outer surface of the work-

piece, with a heat transfer coefficient set at 10 W/m^2·K. In addition, a surface-to-ambient radiation model was activated under high-temperature conditions to account for radiative heat losses from the workpiece to the environment.

The initial temperature of the entire model was set to 298 K. A time-dependent heat transfer solver was used to perform transient thermal simulations, with a total simulation time of 20 minutes. The time step was adaptively controlled to balance computational efficiency and solution accuracy.

To ensure the accuracy of the electromagnetic and temperature field calculations, especially in regions where eddy currents and heat are concentrated (such as the surface of the metal workpiece and areas near the induction coil), a reasonable mesh strategy was employed in the model. In this study, the physics-controlled mesh generation method provided by COMSOL was used, combined with adaptive refinement in critical regions, to create a multi-scale mesh across the entire computational domain.

At the surface of the tantalum workpiece, due to the significant skin effect induced by the high-frequency current excitation, eddy currents primarily concentrate in a thin surface layer, typically on the order of millimeters or smaller. Therefore, a high-density mesh was generated in this region to capture the rapid variations in both current and temperature. In contrast, coarser mesh elements were used in regions farther from the excitation source and in non-critical areas of the structure, in order to reduce the overall computational load and improve simulation efficiency.

To ensure the accuracy of the numerical simulation, a mesh independence verification was conducted using three different mesh densities, consisting of approximately 67991, 131691, and 296302 elements, respectively. Fig. 5 illustrates the temperature evolution of the heated rod over time under each mesh configuration. As shown in the figure, the simulation results obtained using 131691 and 296302 elements are nearly identical, indicating that further mesh refinement has a negligible effect on the outcome. Therefore, considering both computational cost and result accuracy, the mesh with 131691 elements was selected for subsequent simulation studies.

In practical applications, heating efficiency and temperature control precision directly affect the stability of the process and the final performance. As a core energy coupling component in the induction heating system, the structural parameters of the coil have a significant impact on the distribution of the electromagnetic field and the path of eddy currents, which in turn significantly affect the generation of Joule heating and the distribution of the temperature field. Therefore, systematically studying the impact of structural factors, such as the number of coil turns and the distance between the coil and the workpiece, on heating capacity is essential for optimizing the design of induction heating systems and improving heating efficiency and temperature uniformity. This is of great engineering application value and theoretical significance.

To this end, in this study, four different coil structure parameters were simulated and compared under the same excitation current (700 A) and frequency (30 kHz) conditions, with the results shown in Fig. 6. The results clearly demonstrate that the coil structure has a significant impact on both the heating rate and the final temperature. Particularly, when the coil has 3 turns and the distance between the coil and the workpiece is 20 mm, the temperature rises the fastest, with the final stable temperature reaching approximately 1480 K, showing the strongest heating capacity. In contrast, when the coil has 2 turns and the distance between the coil and the workpiece is 30 mm, the temperature rises more slowly, with the final steady-state temperature being only around 1000 K. The average heating rates for the four different coil structures are 118 K/min, 84 K/min, 65 K/min, and 40 K/min, respectively.

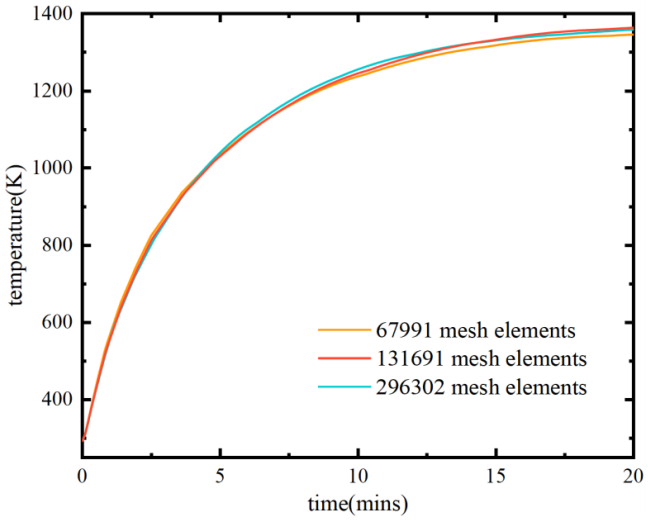

Fig. 5. Grid-independent verification.

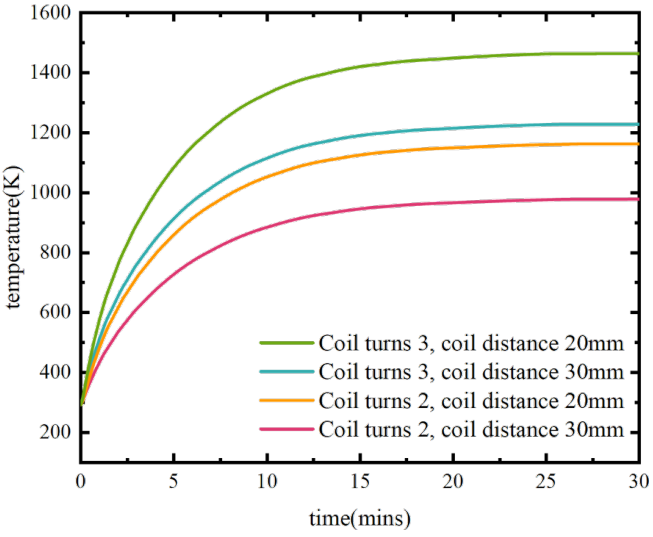

Fig. 6. Coil parameter influence diagram.

The analysis indicates that, under the same conditions, increasing the number of coil turns effectively enhances the intensity of the alternating magnetic field, thereby increasing the induced electromotive force within a unit volume, which

further intensifies the generation of eddy currents and releases more Joule heat. At the same time, reducing the distance between the coil and the workpiece helps improve the coupling efficiency of the magnetic field with the workpiece, allowing the electromagnetic energy to be more efficiently transferred to the metal. Increasing the number of turns or decreasing the distance between the coil and the workpiece not only accelerates the temperature rise rate but also significantly shortens the time required to reach steady-state temperature, indicating a high sensitivity of the induction heating system to structural design optimization.

Therefore, in practical engineering design, the coil configuration with more turns and a smaller distance between the coil and the workpiece should be prioritized, based on specific requirements, to achieve higher heating efficiency and shorter heating times. The results of this study provide strong theoretical support for the structural optimization of induction heating systems and serve as an important reference for achieving precise target temperature control, localized heating, and multi-stage power adjustment.

In the experiment investigating the influence of heating frequency on the performance of an induction heating system, we have selected a coil structure with 2 turns and a 20-millimeter gap between the coil and the workpiece. This selection is based on a comprehensive consideration of multiple factors. From the perspective of coil turns, a 2-turn coil can generate a moderate magnetic field strength while meeting the basic requirements for induction heating. This not only ensures that sufficient eddy currents are induced in the workpiece to achieve heating but also avoids the issues of increased system inductance and reduced power factor that may arise from an excessive number of turns. Moreover, the simplicity of this coil structure facilitates experimental operation and control, reduces experimental costs, and makes heat dissipation easier, thereby contributing to the stable operation of the experimental system. Regarding the gap, the 20-millimeter spacing is carefully designed. This spacing ensures effective magnetic field coupling to the workpiece, preventing local overheating of the workpiece surface due to excessively small gaps and magnetic field energy loss due to excessively large gaps. Additionally, the 20-millimeter spacing accommodates workpieces of various sizes and shapes, enhancing the universality of the experimental results. It also prevents collisions between the workpiece and the coil during the heating process due to thermal expansion, ensuring the safety of the experiment and the stability of the system.

In summary, considering the above factors, we have chosen a coil structure with 2 turns and a 20-millimeter gap between the coil and the workpiece to further investigate the impact of heating frequency on the performance of the induction heating system.To validate the advantages of the 110 kHz high-frequency induction heating device we designed in terms of rapid heating, a comparative analysis was conducted between it and a conventional 30 kHz heating system under the same operating conditions. The study primarily focused on examining the effects of frequency variation on energy coupling efficiency, the distribution of eddy currents within the workpiece, and the rate of temperature rise, in order to reveal the potential benefits of high-frequency induction heating in improving heating response time and thermal efficiency.

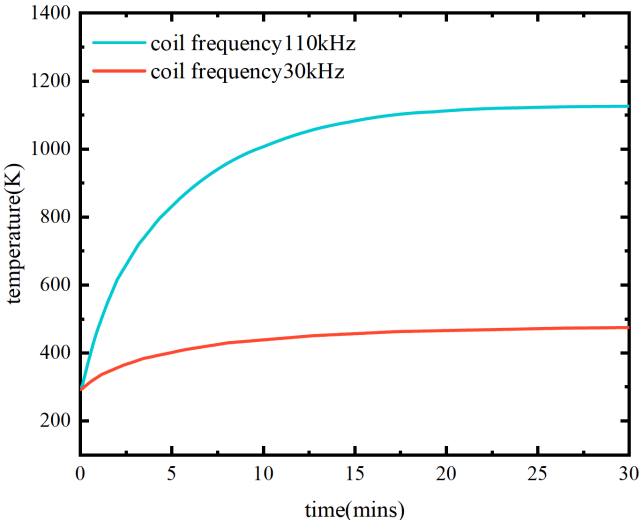

Fig. 7. Comparison of warming processes.

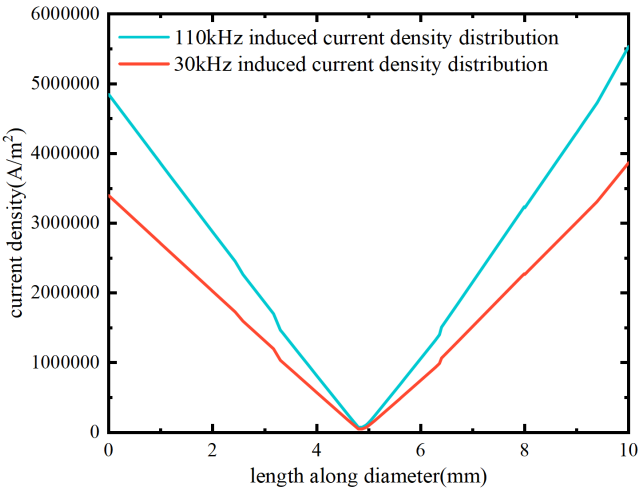

Fig. 8. Comparison of current density distribution.

As depicted in Fig. 7, induction heating at 110 kHz results in a temperature increase of 500 K within the first 5 minutes, which is five times the heating rate under the 30 kHz condition (100 K within the first 5 minutes).Fig. 8 further reveals that the current density peaks at 5.5×10^6 A/m^2 and is confined to the surface layer at 110 kHz, whereas the 30 kHz profile exhibits a lower, more gradual radial decay.This pronounced concentration effect is quantitatively described by the skin effect, for which the characteristic penetration depth is given by $\delta = \sqrt{\rho/\pi f \mu}$. Accounting for the temperature-dependent resistivity of tantalum ($\rho = 156\,\mathrm{n\Omega \cdot m}$ at $T = 500$ K for the 30 kHz case and $\rho = 197\,\mathrm{n\Omega \cdot m}$ at $T = 1100$ K for the 110 kHz case, with the elevated temperature resulting from increased power dissipation), the theoretical skin depths are calculated to be $\delta_{30\,\mathrm{kHz}} = 1.15$ mm

and $\delta_{110\,\mathrm{kHz}} = 0.60$ mm. Despite the higher operating temperature at 110 kHz, which tends to increase the skin depth through elevated resistivity, the dominant frequency dependence reduces the penetration depth by approximately 48%. To validate the agreement between simulated current density and theoretical predictions, the effective skin depth is first defined as the distance over which the alternating current decays to $1/e$ (36.8%) of its surface value within the conductor. δ_{eff} is determined directly from the radial profiles presented in Fig. 8 by identifying the depth at which the current density $J(r)$ falls to J_0/e. This procedure yields $\delta_{\mathrm{eff},30\,\mathrm{kHz}} = 1.18$ mm and $\delta_{\mathrm{eff},110\,\mathrm{kHz}} = 0.62$ mm, which exhibit excellent agreement with theoretical predictions, with deviations within 3%. The enhanced surface concentration substantially increases the heat generation capability. The volumetric heat generation density is given by $q = \rho J^2$, which scales quadratically with current density. At the surface, this yields $q_{30\,\mathrm{kHz}} = 1.6\,\mathrm{MW/m^3}$ and $q_{110\,\mathrm{kHz}} = 5.1\,\mathrm{MW/m^3}$, corresponding to a 3.2-fold enhancement. This significant increase in surface heat flux—achieved despite the operating temperature at 110 kHz exceeding twice that at 30 kHz—enables a doubling of the heating rate from 100 K/5 min to 200 K/5 min. These results validate the efficacy of high-frequency operation for achieving rapid, surface-localized heating. Therefore, increasing the frequency can not only effectively accelerate the heating process but also significantly enhance the skin effect. Under the configuration of 110 kHz, the induction heating efficiency is greatly improved, providing a more efficient and energy-saving solution for relevant applications. To fully and deeply analyze the heating behavior under the 110 kHz configuration, we have conducted multidimensional investigation work. We have not only monitored the dynamic variation trend of the heating power but also measured the steady-state radial temperature distribution along the central diameter direction. In addition, we have carried out a detailed analysis of the corresponding distribution between the overall temperature and the magnetic flux density.

Fig. 9 summarizes the induction-heating behavior at 110 kHz. The panel sequence provides the three-dimensional temperature field, three-dimensional magnetic-flux-density field, two-dimensional temperature contour, two-dimensional magnetic-flux-density contour, instantaneous heating-power curve, and the steady-state temperature distribution along the diameter at the geometric center. In electromagnetic induction heating systems, numerical simulation techniques enable us to analyze the distribution of magnetic flux density and temperature. The transient response of the heating power curve at system startup, although initially exhibiting an overshoot phenomenon, rapidly decays within a certain timeframe, demonstrating the system's ability to quickly achieve electromagnetic-thermal equilibrium. The radial temperature distribution features a typical saddle shape, which is the result of the combined effects of surface convection cooling and axial heat conduction, with the surface forming a shallow temperature minimum due to convective heat dissipation. This temperature distribution characteristic is crucial for understanding and predicting the thermodynamic behavior during the heating process and also confirms the rapid establishment of electromagnetic-thermal equilibrium, which is of significant importance for improving heating efficiency and ensuring heating quality. To further validate the rapid-heating capability of the developed induction system, an experimental campaign was conducted under identical operating conditions.

IV. INDUCTION HEATING EXPERIMENTAL TEST

To evaluate the rapid heating performance of the designed induction heating system, an experimental platform was established in this study, as illustrated in Fig. 10. This platform was specifically developed to systematically verify the heating efficiency of the high-frequency induction system and to enable the synchronized control of heating and mechanical loading processes. The platform integrates a high- frequency induction heating module, a mechanical loading unit, a precision temperature monitoring system, a closed-loop water cooling system, and a supervisory control platform, providing a stable and high-responsive testing environment for high-temperature thermomechanical coupling experiments.

Before each experiment , a comprehensive inspection and preheating of the equipment were conducted to ensure the proper operation of all modules. Special attention was given to the induction heating system's power supply, coil, water cooling system pipes, and temperature control system, all of which underwent rigorous checks to prevent issues such as overheating or energy overload during the experiment. Simultaneously, the mechanical loading system was calibrated to confirm that its loading accuracy and range meet the experimental requirements. During this process, the surface of the specimen was cleaned and polished to remove oxides and oil, ensuring the accuracy and consistency of both temperature measurement and mechanical loading.

Once the experiment began, the induction heating system was activated, and the output frequency and power of the power supply were set. The specimen was then heated by induction via a 2-turn copper coil. At the frequency of 110 kHz, the system rapidly heated the specimen surface to the desired temperature (typically between 1000 K and 1400 K), with temperature accuracy monitored in real time. To reduce interference during temperature measurement, the system was equipped with an infrared non-contact temperature sensor and a K-type thermocouple, and the real-time data were fed back to the control platform for calibration and validation. Temperature data were recorded every second to ensure continuous monitoring of dynamic temperature changes, and the system adjusted relevant heating parameters, such as heating rate and target temperature,according to the experimental requirements. Additionally, power, frequency, and other electrical parameters of the induction heating process were recorded synchronously for subsequent data analysis and verification.

Once the induction heating system reached stable operation, the mechanical loading system was activated. The loading force started from 0 N and gradually increased. The loading process was precisely controlled by an electronic servo universal testing machine, which applies axial tension

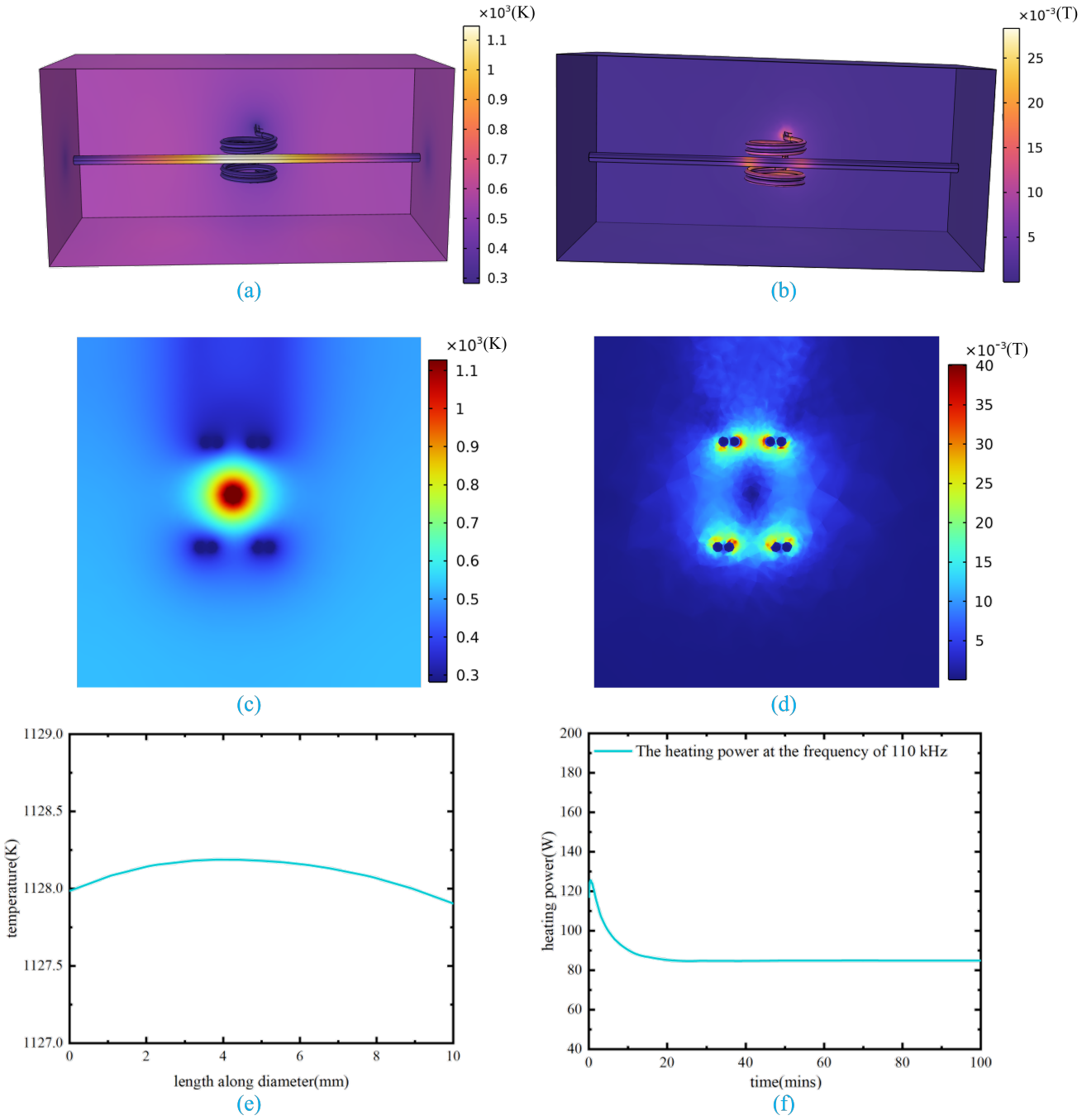

Fig. 9. Performance analysis of 110 kHz induction heating:(a) 3D temperature distribution,(b) 3D magnetic flux density distribution,(c) 2D temperature distribution,(d) 2D magnetic flux density distribution,(e) Center-line temperature profile along the diameter,(f) Heating power evolution.

or compression at a set rate , with the loading modes selected according to the experimental design. All force and displacement data were continuously collected by sensors throughout the loading phase, ensuring parameter accuracy and consistency.

The core of the experiment was the thermomechanical coupling process, during which high temperature and mechanical loading acted simultaneously on the specimen to simulate real-world working conditions. The high-frequency current generated a strong skin effect, causing the specimen's surface temperature to rise rapidly. Concurrently, due to the applied mechanical loading, the specimen underwent deformation, and the material's microstructure, strength, and deformation behavior changed significantly with varying temperature and stress. Once the experiment reached the predetermined duration, the loading process ended, and the induc-

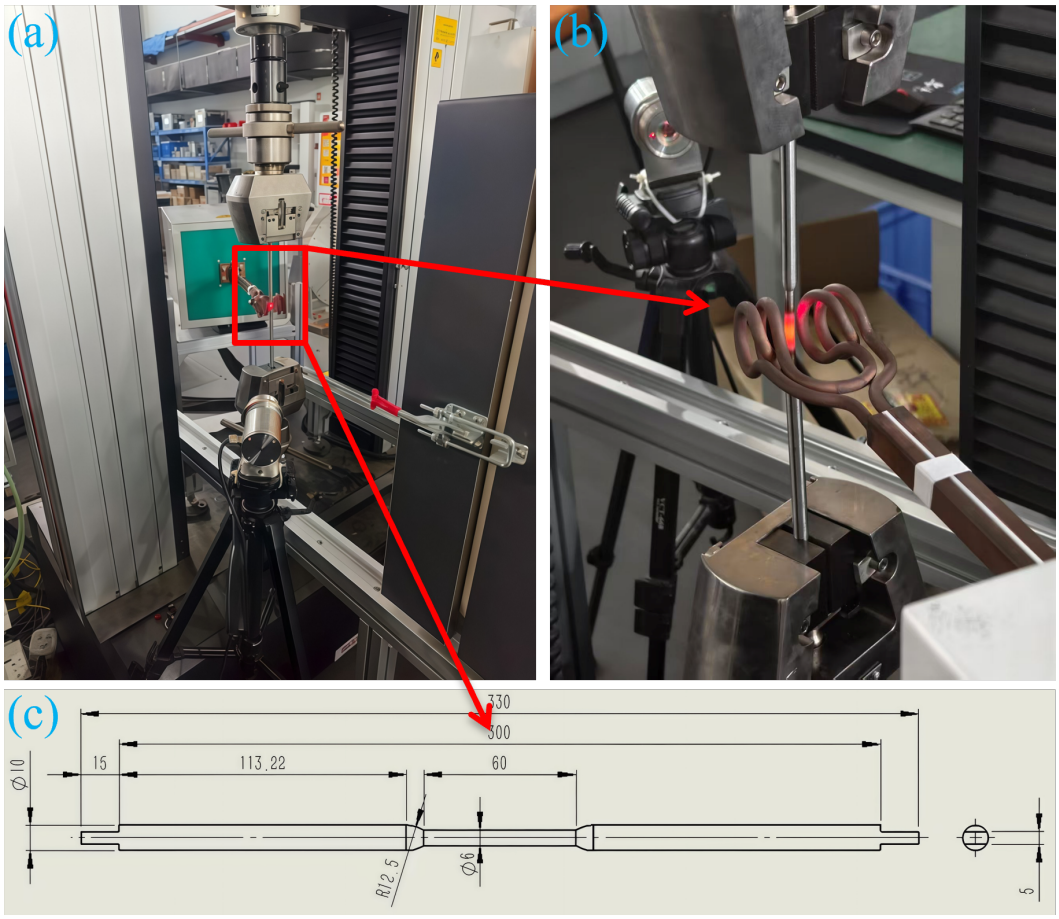

Fig. 10. Experimental platform: (a) High-Temperature In-Situ Experimental Platform; (b) Schematic diagram of heating localization; (c) Dimensions of Bar-Shaped Specimens.

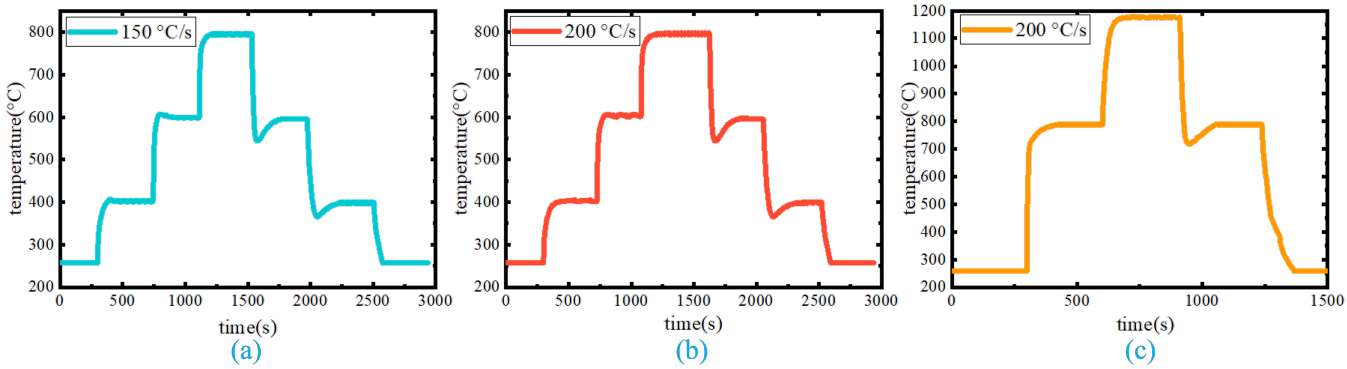

Fig. 11. Test of temperature control stability under different heating rates: (a) The system heats at 150 °C/s until reaching 800 °C; (b) The system heats at 200 °C/s until reaching 800 °C.; (c) The system heats at 200 °C/s until reaching 1200 °C.

tion heating system was turned off, completing the thermo-mechanical coupling experiment.

To comprehensively validate the system's real-time temperature control performance and the claimed high heating rates, we designed and conducted a series of precise closed-loop control experiments. As shown in Fig. 11, the system demonstrated excellent dynamic response and stability. We performed closed-loop control tests with different heating rates (150°C/s, 200°C/s) targeting setpoint temperatures of 400°C, 600°C, and 800°C, and further carried out closed-cycle tests at heating rate of 200°C/s target of 800°C and 1200°C. These experiments simulated complex heat treat-

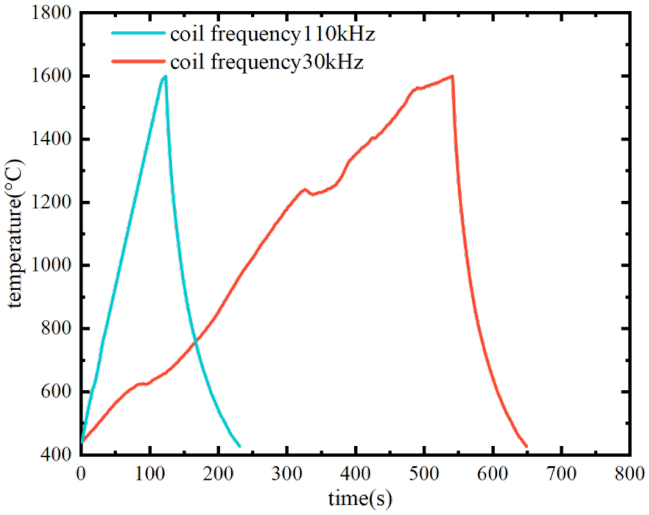

Fig. 12. Comparison of heating rates at different frequencies .

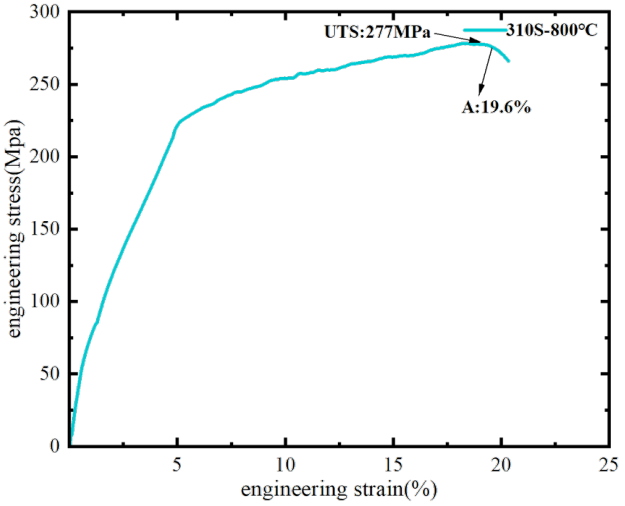

Fig. 13. High-Temperature Mechanical Properties of Specimens .

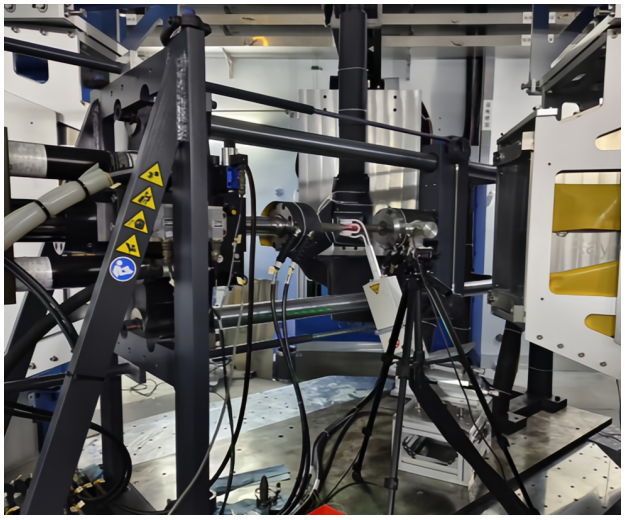

Fig. 14. Induction heating equipment coupled with stress loading frame installed in Engineering Material Neutron Diffractometer at CSNS.

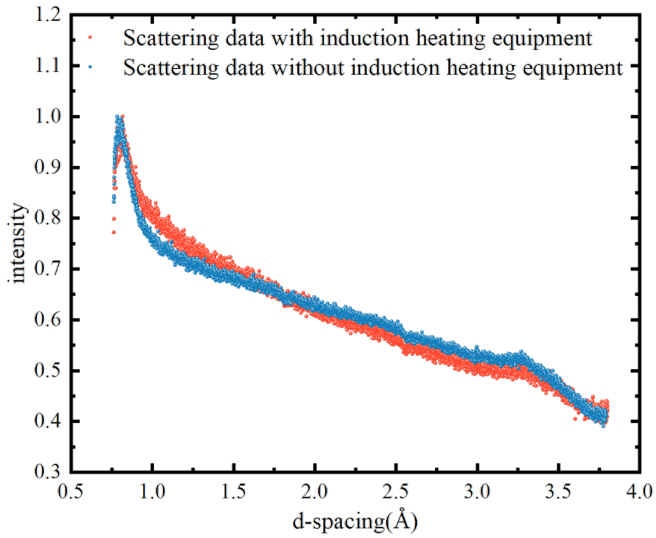

Fig. 15. Comparison of neutron scattering results with and without induction heating equipment .

ment processes, including stepwise heating, precise dwell periods, and subsequent cooling stages.

The temperature-time curves show that the system responds rapidly to each heating command, achieving a temperature rise of several hundred degrees Celsius in a short time, confirming its capability for rapid heating rates of up to 200°C/s. Notably, this peak rate occurred primarily during the initial heating phase when the system's thermal inertia was low, allowing the controller to deliver maximum power. As the temperature approached the target setpoint, the PID closed-loop control algorithm adjusted the heating power to prevent overshoot caused by thermal inertia, enabling the temperature curve to smoothly approach and stabilize at the setpoint and without overshoot. This demonstrates the advantage of "fast start-up, precise stabilization" inherent in closed-loop control.

Once the temperature reached plateaus such as 800°C and higher, the system quickly entered a stable state, with temperature fluctuations confined to a narrow range, showcasing high-precision temperature maintenance. Throughout the multi-stage cycle, the temperature curve remained smooth, continuous, and repeatable, with no abnormal deviations, confirming the system's operational stability and reliability under complex, long-duration thermal cycling.

Furthermore, analysis of the high-temperature data, particularly above 800°C, revealed slight, gradual in the temperature curve. This was primarily due to surface oxidation of the heating element (tantalum rod) at high temperatures under the laboratory test conditions, leading to drift in its resistive properties and thereby introducing minor inaccuracies in the temperature feedback. It is important to note that in the

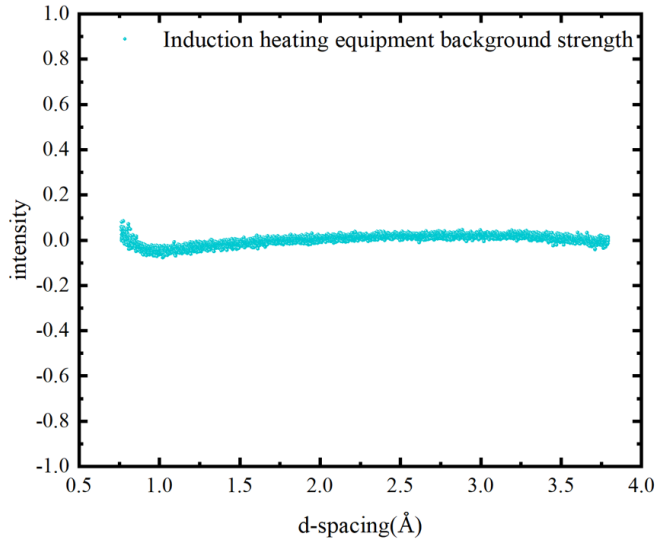

Fig. 16. Induction heating equipment background strength .

actual spectrometer environment, the sample chamber operates under a high-purity inert gas atmosphere,such as argon, which eliminates oxygen exposure, thereby preventing high-temperature oxidation and ensuring long-term measurement and control accuracy across the entire temperature range.

To systematically compare the rapid heating performance, a frequency comparison group was conducted, using identical coil structures and a prescribed heating rate of 10 °C/s at frequencies of 110 kHz and 30 kHz. As shown in Fig. 12, the experimental results indicate that at 110 kHz, the induction heating system heated the specimen to the target temperature in a shorter time and at a higher heating rate. Under high-frequency excitation, the skin effect was enhanced, resulting in a higher density of circulating currents on the specimen's surface. This effect significantly increased the power density of Joule heating, thereby improving the efficiency of heat energy input. This characteristic not only accelerated specimen heating but also provided a stable high-temperature environment for the subsequent loading process, ensuring the stability and consistency of the heating procedure.

Subsequently, to evaluate the feasibility of force-thermal loading, we conducted an experiment on 310S stainless steel under force-thermal conditions, as depicted in Fig. 13, which illustrates the stress-strain curve obtained at 800°C.It should be noted that the tantalum rods used previously served only as reference samples for temperature calibration. For the formal mechanical performance tests, 310S stainless steel was selected because it has excellent oxidation resistance, microstructural stability, and repeatable mechanical behavior at high temperatures, making it more suitable for constitutive characterization under force-heat coupling loads. This curve captures the entire deformation process of the material, from the elastic to the plastic phase and ultimately fracture. At the onset, the curve exhibits a steep slope, indicating elastic behavior. As strain progresses, the slope diminishes gradually, signifying the onset of plastic deformation where the rate of stress increment slows down. The curve reveals a yield strength of 277 MPa for the material, beyond which a decline is observed, signifying the initiation of necking prior to fracture. Additionally, the curve denotes a fracture elongation of 19.6%, reflecting the ductility of the material before rupture. These results are important for evaluating the mechanical properties of 310S stainless steel at high-temperature conditions, particularly in studies requiring precise temperature control and rapid thermal response, such as dynamic high-temperature loading, stress measurement, and in-situ monitoring of material behavior.

In neutron scattering experiments, it is crucial to ensure that the induction heating device does not significantly affect the scattering results of the sample. To this end, we designed an experiment to assess whether the introduction of the induction heating device would generate additional diffraction peaks in the scattering pattern,The experimental setup is shown in Fig. 14. In the experiment, vanadium-nickel alloy samples were tested, and neutron scattering data were recorded by the materials testing system (MTS) and the induction heating device, as well as under the MTS alone, as shown in Fig. 15." Both curves were normalized to their respective maximum intensities to enable direct comparison of the spectral features.By subtracting the control group data from the experimental group data, we were able to isolate the scattering signals from other devices, thereby revealing the scattering contribution of the induction heating device. As shown in Fig. 16, the difference analysis produced a line close to zero, indicating that the induction-heating device introduced no additional diffraction peaks and had no significant effect on the scattering pattern of the samples. These experimental results confirm that the induction heating device we designed had no significant impact on the scattering results of vanadium-nickel alloy samples in neutron scattering experiments, and introduced no additional diffraction peaks. This conclusion not only supports the reliability of the induction heating device but also provides an important reference for future high-temperature mechanical property tests.

V. SUMMARY

This study presents a high-frequency induction heating for rapid and precise temperature. Through theoretical analysis, simulation studies, and experimental verification, the scheme has demonstrated significant improvements in heating rate and temperature control accuracy, effectively overcoming key limitations of conventional heating systems. By increasing the frequency to 110 kHz and employing a high-current zero-current switching (ZCS) IGBT series resonant converter, this study has successfully achieved efficient compression of electromagnetic energy into the submillimeter surface layer. This increased both thermal flux density and heating rate. Both simulation and experimental results show that, under the same power conditions, the high-frequency heating technology can rapidly heat samples to higher temperatures. For the same target temperature, the technology exhibits a faster heating rate and higher stability. This characteristic is crucial for in situ

characterization experiments, as it provides repeatable and precise temperature profiles, thereby improving the temporal resolution and data quality .In neutron scattering experiments, the induction heating device designed in this study exhibits low background characteristics, making it suitable for neutron diffractometers application, without compromising data the integrity and accuracy of sample data. Compared with traditional low-frequency heating systems, the high-frequency technology adopted in this study offers clear advantages in energy efficiency and control accuracy. The technology has broad application prospects and significant engineering value in low-carbon precision heat treatment, high-temperature material testing, and advanced in situ characterization.

[1] M. L. Grilli, D. Valerini, A. E. Slobozeanu et al., Critical raw materials saving by protective coatings under extreme conditions: A review of last trends in alloys and coatings for aerospace engine applications. *Materials* **14**, 1656 (2021). doi: 10.3390/ma14071656

[2] H. A. Zeid and H. Elshahawi, Where Deep Space Meets the Deep Ocean–Exploring the Extreme Environments of Space and Deepwater. In: Offshore Technology Conference (OTC), Houston, TX, USA, April 2024 [Paper D021S021R001].

[3] C. Deng, S. J. Wang, Q. Hu, et al., Deep learning-based compressed sampling reconstruction algorithm for digitizing intensive neutron ToF signals. *Nucl. Sci. Tech.* **36**(7), 112 (2025). doi: 10.1007/s41365-025-01669-5

[4] V. A. Varlachev, E. G. Emets, Y. C. Mu, et al., Determining absolute value of thermal neutron flux density based on monocrystalline silicon in nuclear reactors. *Nucl. Sci. Tech.* **33**, 83 (2022). doi: 10.1007/s41365-022-01077-z

[5] J. C. Wang, J. Ren, W. Jiang, et al., In-beam gamma rays of CSNS Back-n characterized by black resonance filter. *Nucl. Sci. Tech.* **35**(10), 38 (2024). doi: 10.1007/s41365-024-01553-8

[6] B. Jiang, B. B. Tian, H. T. Jing, et al., Feasibility of medical radioisotope production based on the proton beams at China Spallation Neutron Source. *Nucl. Sci. Tech.* **35**(6), 38 (2024). doi: 10.1007/s41365-024-01438-w

[7] Z. Zhang, C. B. Meng, X. L. Jiang, et al., Comprehensive quality assessment method for neutron radiographic images based on CNN and visual salience. *Nucl. Sci. Tech.* **36**, 118 (2025). doi: 10.1007/s41365-025-01686-4

[8] J. J. Ma, F. Q. Zhou, X. J. Sun, et al., Activation cross sections for reactions induced by 14 MeV neutrons on natural copper. *Nucl. Sci. Tech.* **29**, 150 (2018). doi: 10.1007/s41365-018-0485-y

[9] K. Z. Xu, Y. B. Nie, C. L. Lan, et al., Integral experiment on slab natPb using D-T and D-D neutron sources to validate evaluated nuclear data. *Nucl. Sci. Tech.* **36**, 49 (2025). doi: 10.1007/s41365-024-01623-x

[10] X. F. Jiang, J. R. Zhou, H. Luo, et al., A large area 3He tube array detector with vacuum operation capacity for the SANS instrument at the CSNS. *Nucl. Sci. Tech.* **33**, 89 (2022). doi: 10.1007/s41365-022-01067-1

[11] S. H. Zhao, H. Huang, Z. Y. Wan, et al., Development of readout electronics for high resolution neutron scintillator detector. *Nucl. Tech.* **46**(11), 33-42 (2024).

[12] T. Y. Honh, Y. P. Song, L. P. Zhou, et al., Beamline design for multipurpose muon beams at CSNS EMuS. *Nucl. Sci. Tech.* **35**(5), 38 (2024). doi: 10.1007/s41365-024-01406-4

[13] P. Sengupta and I. Manna, Advanced high-temperature structural materials in petrochemical, metallurgical, power, and aerospace sectors—An overview. In: Future landscape of structural materials in India, Singapore: Springer, 2022, pp. 79-131.

[14] G. G. Goviazin, J. C. Nieto-Fuentes and D. Rittel, Review: High Speed Temperature Measurements Under Dynamic Loading. *Exp. Mech.* **64**, 295-304 (2024). doi: 10.1007/s11340-023-01027-9

[15] M. Kawasaki, J. K. Han, X. Liu et al., In situ heating neutron and X-ray diffraction analyses for revealing structural evolution during postprinting treatments of additive-manufactured 316L stainless steel. *Adv. Eng. Mater.* **24**, 2100968 (2022). doi: 10.1002/adem.202100968

[16] H. Nozaki, H. Kondo, T. Shinohara et al., In situ neutron imaging of lithium-ion batteries during heating to thermal runaway. *Sci. Rep.* **13**, 22082 (2023). doi: 10.1038/s41598-023-49399-1

[17] Q. Zheng and T. Furushima, Evaluation of high-temperature tensile behavior for metal foils by a novel resistance heating assisted tensile testing system using samples with optimized structures. *J. Mater. Sci. Technol.* **94**, 216-229 (2021) (in Chinese). doi: 10.1109/TASC.2020.2971954

[18] X. Wang, X. Xie, W. Yu, et al., Hot-zone design and optimization of resistive heater for SiC single crystal growth. *J. Mater. Sci.* **59**, 8930-8941 (2024). doi: 10.1007/s10853-024-09717-y

[19] B. Lv, Y. Liu, W. Wu, et al., Local large temperature difference and ultra-wideband photothermoelectric response of the silver nanostructure film/carbon nanotube film heterostructure. *Nat. Commun.* **13**, 1835 (2022). doi: 10.1038/s41467-022-29455-6

[20] D. Fan, W. Zhou, S. Wei, et al., A simple external resistance heating diamond anvil cell and its application for synchrotron radiation X-ray diffraction. *Rev. Sci. Instrum.* **81**, 053903 (2010). doi: 10.1063/1.3428827

[21] C. Liu, M. Li, Y. Gu, et al., Resistance heating forming process based on carbon fiber veil for continuous glass fiber reinforced polypropylene. *J. Reinforced Plast. Compos.* **37**, 366-380 (2018). doi: 10.1177/0731684417751058

[22] J. Mills-Brown, K. Potter, S. Foster et al., The development of a high temperature tensile testing rig for composite laminates. *Compos. Part A Appl. Sci. Manuf.* **52**, 99-105 (2013). doi: 10.1016/j.compositesa.2013.04.009

[23] A. Wang, H. D. Tolley and M. L. Lee, Gas chromatography using resistive heating technology. *J. Chromatogr. A* **1261**, 46-57 (2012). doi: 10.1016/j.chroma.2012.05.021

[24] X. Li, Y. Yang, Z. Quan, et al., Tailoring body surface infrared radiation behavior through colored nanofibers for efficient passive radiative heating textiles. *Chem. Eng. J.* **430**, 133093 (2022). doi: 10.1016/j.cej.2021.133093

[25] S. Lupi, M. Forzan and A. Aliferov, Induction and direct resistance heating. Switzerland: Springer, 2015.

[26] Y. S. Du, Q. Lin, W. Ye, et al., The Kinetic Effects of Different Rare-earth Additives on the Oxidation Resistance of$Ni_{80}Cr_{20}$ Alloy. *Chinese J. Eng.* **13**, 267-272 (1991). doi: 10.13374/j.issn1001-053x.1991.03.030

[27] K. Y. Zhang, B. Liu, Y. Lei et al., An iterative algorithm to improve infrared thermographic systems' accuracy in temperature field measurement of aluminum alloys. *Measurement* **210**,

112547 (2023). doi: 10.1016/j.measurement.2023.112547

[28] T. Wang, L. Xia, M. Ni, et al., Fundamentals of infrared heating and their application in thermosetting polymer curing: a review. *Coatings* **14**, 875 (2024). doi: 10.3390/coatings14070875

[29] O. Lucía, P. Maussion, E. J. Dede et al., Induction heating technology and its applications: Past developments, current technology, and future challenges. *IEEE Trans. Ind. Electron.* **61**, 2509-2520 (2014). doi: 10.1109/TIE.2013.2281162

[30] T. Wang, F. Bai, P. Yao, et al., Experimental study of electromagnetic induction heating ceramic particles device (EI-HCPD). *Energy Convers. Manag.* **345**, 120398 (2025). doi: 10.1016/j.enconman.2025.120398

[31] L. Siesing, F. Lundström, K. Frogner et al., Towards energy efficient heating in industrial processes—Three steps to achieve maximized efficiency in an induction heating system. *Procedia Manuf.* **25**, 404-411 (2018). doi: 10.1016/j.promfg.2018.06.110

[32] J. Dong, Z. Zhang, D. Wang, et al., Numerical simulation and experimental study on the preparation of the inner layer of bimetal composite pipe by high-frequency induction heating. *Mater. Today Commun.* **38**, 108118 (2024). doi: 10.1016/j.mtcomm.2024.108118

[33] P. Yang, S. T. Dai, T. Ma et al., Heating Characteristic and Thermal Optimization of Superconducting DC Induction Heater With Adjustable Air Gap Structure. *IEEE Trans. Appl. Supercond.* **30**, 4601607 (2020). doi: 10.1109/TASC.2020.2971954

[34] B. Barman and M. Sengupta, Parameter Determination of a Multi-layered Induction Heating Coil: Analytical, Simulation and Experimental Studies. *J. Inst. Eng. (India): Ser. B* **105**, 1299-1317 (2024). doi: 10.1007/s40031-024-01000-7

[35] R. Haynes, A. M. Paradowska, M. A. H. Chowdhury et al., An inert-gas furnace for neutron scattering measurements of internal stresses in engineering materials. *Meas. Sci. Technol.* **23**, 047002 (2012). doi: 10.1088/0957-0233/23/4/047002

[36] O. Kirichek, Sample environment for neutron scattering experiments at ISIS. *J. Neutron Res.* **20**, 57-63 (2017). doi: 10.1080/10448632.2019.1605791

[37] K. An, Y. Chen, A. D. Stoica, et al., VULCAN: A "hammer" for high-temperature materials research. *MRS Bull.* **44**, 878-885 (2019). doi: 10.1557/mrs.2019.256

[38] O. Kirichek, Technical report on ultra-low temperature sample environment for neutron scattering at ISIS. *Neutron News* **30**, 11-13 (2019). doi: 10.1080/10448632.2019.1605790

[39] L. J. Deng, H. Cheng, F. Ye, et al., Investigation on the temperature characteristics of a laser heating furnace for neutron scattering experiments at CSNS. *Nucl. Instrum. Methods Phys. Res. A* **1081**, 170900 (2026). doi: 10.1016/j.nima.2025.170900

[40] H. Cheng, H. T. Hu, C. M. Hu, et al., An ultra-high temperature furnace for temperature determination by neutron resonance spectroscopy. *Nucl. Instrum. Methods Phys. Res. A* **1049**, 168072 (2023). doi: 10.1016/j.nima.2023.168072

[41] A. Smith, B. Jones, C. Williams, et al., High-temperature performance of advanced ceramics in inductive heating environments. *Adv. Appl. Ceram.* **110**, 589-603 (2010). doi: 10.1179/1743284710Y.0000000029

[42] J. R. Santisteban, L. Edwards, M. E. Fitzpatrick, et al., Strain imaging by Bragg edge neutron transmission. *Nucl. Instrum. Methods Phys. Res. A* **481**, 765-768 (2002). doi: 10.1016/S0168-9002(01)01256-6

[43] B. Drobenko, O. Hachkevych, T. Kournyts'kyi, A mathematical simulation of high temperature induction heating of electroconductive solids. *Int. J. Heat Mass Transf.* **50**(3), 616–624 (2007). doi: 10.1016/j.ijheatmasstransfer.2006.07.013